POLITECNICO DI TORINO
Repository ISTITUZIONALE

Influence of the annealing and defects on the VHCF behavior of an SLM AlSi10Mg alloy

(Article begins on next page)

25 April 2024

Influence of the annealing and defects on the VHCF behaviour of an SLM AlSi10Mg alloy

Authors:

A. Tridello[a], J. Fiocchi[b], C.A. Biffi[c], G. Chiandussi[d], M. Rossetto[e], A. Tuissi[f], D.S. Paolino[g]

[a] Department of Mechanical and Aerospace Engineering, Politecnico di Torino, 10129 Turin, Italy,
andrea.tridello@polito.it
[b] CNR ICMATE – Institute of Condensed Matter Chemistry and Technologies for Energy, 23900 Lecco, Italy,
jacopo.fiocchi@icmate.cnr.it
[c] CNR ICMATE – Institute of Condensed Matter Chemistry and Technologies for Energy, 23900 Lecco, Italy,
carloalberto.biffi@cnr.it
[d] Department of Mechanical and Aerospace Engineering, Politecnico di Torino, 10129 Turin, Italy,
giorgio.chiandussi@polito.it
[e] Department of Mechanical and Aerospace Engineering, Politecnico di Torino, 10129 Turin, Italy,
massimo.rossetto@polito.it
[f] CNR ICMATE – Institute of Condensed Matter Chemistry and Technologies for Energy, 23900 Lecco, Italy,
ausonio.tuissi@cnr.it
[g] Department of Mechanical and Aerospace Engineering, Politecnico di Torino, 10129 Turin, Italy,
davide.paolino@polito.it

Corresponding Author:

A. Tridello
E-mail address: andrea.tridello@polito.it
Full postal address:
C.so Duca degli Abruzzi 24,
Department of Mechanical and Aerospace Engineering – Politecnico di Torino,
10129 – Turin,
ITALY
Phone number: +39.011.090.6913
Fax number: +39.011.090.6999

Abstract:

In the paper, the influence of the annealing temperature on the Very-High-Cycle-Fatigue, VHCF, of AlSi10Mg specimens produced through Selective Laser Melting (SLM) is experimentally assessed. VHCF tests at 20 kHz are carried out on Gaussian specimens subjected to a heat treatment suggested by the system supplier (heating for 2 hours to 320°C and air cooling) and to a heat treatment proposed by the authors (heating for 2 hours to 244°C and air cooling). The defects originating failure and the conditional P-S-N curves are compared. Experimental results show that an annealing temperature of 320°C induces the spheroidization of the Si network, which enhances the ductility but has a negative effect on the VHCF response. On the contrary, by reducing the heating temperature to 244°C, the original as-built microstructure is not altered and the minimization of the residual stresses permits to enhance the VHCF response.

Acronyms and nomenclature

AM: Additive Manufacturing

SLM: Selective Laser Melting

VHCF: Very-High-Cycle-Fatigue

AB: as-built

HT-320: suggested heat treatment

HT-244: heat treatment proposed by the authors

σ_s: yield stress

σ_u: ultimate tensile strength

ε_f: elongation to failure

HV: Vickers hardness

s_{center}: stress amplitude at the specimen center (calibration gage)

s_{horn}: stress amplitude measured by the gage bonded to the horn (control gage)

s_{local}: local stress amplitude, stress amplitude at the defect location.

N_f: number of cycles to failure.

SIF: Stress Intensity Factor

$\sqrt{a_c}$: square root of the projected area of the defect originating failure (critical defect)

K_{th}: SIF threshold

1. INTRODUCTION

In the last few years, the research on the fatigue response of components produced by Additive Manufacturing (AM) processes has gained significant attention among researchers and industries[1]. Experimental results showed that as-built components produced by different AM processes, such as Selective Laser Melting (SLM) or Electron Beam Melting (EBM), are characterized by a fatigue response below that of parts obtained by conventional manufacturing processes (wrought parts)[2-4]. The high surface roughness[5-7], as well as large internal defects originating during the consolidation of the powder[7-9] are the main reasons for the reduced fatigue response of as-built AM parts. In addition, the fine microstructure typical of AM parts, ensuring quasi-static mechanical properties comparable or even better than those of wrought parts, contributes to limit the fatigue response since a very fine microstructure is less effective in delaying or stopping crack propagation[10]. Accordingly, in order to obtain AM parts characterized by a fatigue response comparable to that of wrought parts and to extend the use of these parts even for applications where fatigue loads are critical, the interactions between surface roughness, defects and microstructure should be properly experimentally assessed and investigated.

Many solutions have been proposed with the aim of improving the fatigue response of AM parts. A proper choice of the process parameters and of the scanning strategy permits to reduce the surface roughness[10] and to limit the size of internal defects[10, 11] in the SLM process. Post-process treatments can be also effectively adopted: for instance, by removing a thin layer of material through machining, the surface roughness can be controlled and surface defects[6] can be eliminated, whereas the Hot Isostatic Pressing (HIP) can be usefully exploited to reduce internal porosities, enhancing the fatigue response[4, 12]. Heat treatments can also be applied to limit and minimize residual stresses and to modify the microstructure of the AM part[13-16]. The influence on the mechanical properties of the microstructural modifications induced by a heat treatment and the interactions between the microstructure and the defects are subjects of primary importance among researchers and industries working in the AM field. In particular, the effect of different heat treatments on the High-Cycle-Fatigue (HCF) response has been quite extensively investigated in the literature[13-16]. On the contrary, there are still few results on the effect of heat treatments on the Very-High-Cycle-Fatigue (VHCF)[17-19], even though, in an increasing number of applications, components are required to bear cyclic loads for number of cycles in the range 10^7 - 10^9.

In the paper, the influence of the annealing temperature on the fatigue response up to 10^9 cycles of SLM AlSi10Mg specimens is experimentally assessed. Ultrasonic tests (20 kHz loading frequency) are performed with the ultrasonic testing machines available at DynLab in Politecnico di Torino[20]. Tests are carried out on Gaussian specimens with large risk-volume[21-23]. Specimens are subjected to the heat treatment suggested by the system supplier[24] (heating for 2 hours to 320°C and air cooling to room temperature[25, 26]) and to a heat treatment proposed by the authors (heating for 2 hours to 244°C and air cooling to room temperature[26]). The mechanical properties of the annealed specimens are compared with those assessed on specimens in

the as-built condition (not annealed)[27]. Fracture surfaces are observed by using the optical microscope and the Scanning Electron Microscope (SEM) to analyze and compare the defects originating the fatigue crack (type, morphology and size) and to investigate the interaction between the microstructure and the defects on the fatigue crack growth and propagation in the VHCF region. Finally, starting from the defect size distribution, the P-S-N curves are estimated and compared to assess the effect of the investigated low temperature heat treatments and of the resulting microstructure on the VHCF response.

2. EXPERIMENTAL ACTIVITY

In Subsection 2.1 the AlSi10Mg powder and annealing characteristics are reported. In Subsection 2.2 the tensile properties and the Vickers hardness are compared. Finally, in Subsection 2.3 the ultrasonic VHCF testing configuration is described. In the following, *AB* specimen will refer to the as-built specimen; *HT-320* specimen will refer to the specimen subjected to the heat treatment suggested by the supplier; *HT-244* specimen will refer to the specimen subjected to the relatively good heat treatment proposed by the Authors.

2.1 AlSi10Mg powder and annealing characteristics

Specimens were built in the horizontal orientation (x-y plane[28]) by using spherical gas atomized AlSi10Mg powders (mean size of $45\,\mu m$, dimensional range between $20 - 63\,\mu m$) and a Selective Laser Melting machine (SLM Solutions, 500 HL quad $4 \times 400\,W$). The building platform was heated to $150\,°C$ (input parameter in the SLM system). Table 1 summarizes the AlSi10Mg powder[29] chemical composition and the process parameters considered for the manufacturing of the specimens: the local energy density was equal to 50,8 J/mm^3 and the approximate build rate equal to 35 cm^3/h.

AlSi10Mg powder chemical composition							
Si	**Mg**	**Cu**	**Ni**	**Fe**	**Mn**	**Ti**	**Al**
10	0.4	< 0.25	< 0.05	< 0.25	< 0.1	< 0.15	bal

SLM process parameters					
Power	*Plate temperature*	*Scanning speed*	*Spot size*	*Hatch distance*	*Layer thickness*
350 W	$150\,°C$	$1.15\ m/s$	$80\,\mu m$	$170\,\mu m$	$50\,\mu m$

Table 1: AlSi10Mg powder (wt. %) and SLM process parameters.

After the manufacturing process, two annealing heat treatments were applied to the produced specimens. The first one was suggested by the AM system manufacturer[25, 26] for the relief of the residual stress and the homogenization of the microstructure. It involves annealing for two hours at 320 °C and air cooling to room temperature. The second heat treatment was originally proposed by the authors in Ref.[26]. It is aimed at obtaining a balanced set of mechanical properties by contemporarily stress relieving the part and inducing

the precipitation of the strengthening phase β''. For this heat treatment, the annealing temperature was reduced to 244 °C (2 hours), followed by air cooling to room temperature.

The microstructure of the AB, of the HT-320 and of the HT-244 specimens was deeply investigated in Ref.[24, 26, 30] and is depicted in Fig. 1 (SEM, mod. Leo 1413). Please refer to Ref. [24, 26, 30] for more details on the microstructural properties of the specimens in the three investigated conditions.
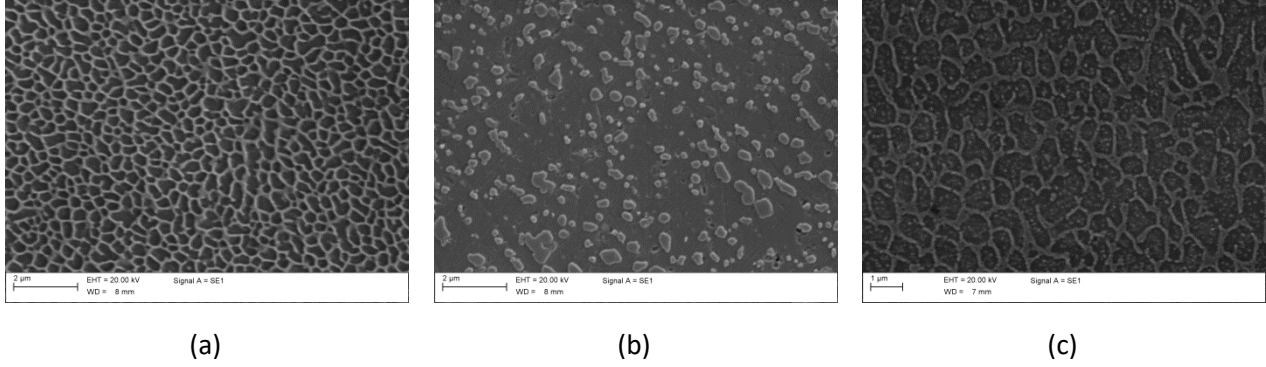

(a) (b) (c)

Figure 1: SEM micrographs of the AlSi10Mg parts in the three investigated conditions: AB (a) HT-320 (b) and HT-244 (c) specimens along the x-y plane.

2.2. Tensile strength and Vickers hardness

The effect of the annealing temperature on the quasi static mechanical properties was at first assessed through tensile tests on dog-bone specimens (three for each condition) by using an MTS 2/M machine and an extensometer for measuring the strain. Table 2 summarizes the measured yield stress, σ_s, tensile strength, σ_u, and elongation to failure, ε_f.

	σ_s [MPa]	σ_u [MPa]	ε_f [%]
AB	287 ($\pm$ 5)	413 ($\pm$ 7)	5.5 ($\pm$ 0.1)
HT-320	142 ($\pm$ 5)	234 ($\pm$ 7)	13.4 ($\pm$ 0.1)
HT-244	232 ($\pm$ 5)	344 ($\pm$ 3)	4.2 ($\pm$ 0.2)

Table 2: Quasi static properties of AB, HT-320 and HT-244 specimens.

It may be clearly appreciated that both heat treatments lower the σ_u: for the HT-320 specimens, the tensile strength is almost half of that measured in AB specimens. The lower annealing temperature treatment was able to retain higher strength thanks to the absence of the Si network spheroidization, and, at the same time, it allows for a significant reduction of the residual stresses, as reported in Ref.[31, 32]. Ductility was significantly improved (from 5.5% to 13.4%) by annealing at 320 °C, whereas it was slightly lowered in HT-244 specimens

(4.2%). This behavior is thought to be caused by the formation of semi-coherent β' phases, which are known to detrimentally affect elongation to failure. However, it should be noted that this value is still higher than the one usually exhibited by the same alloy produced by casting[33].

The tensile strength obtained experimentally can be compared with that obtained in the literature. In particular, in Ref.[15] experimental tests on AlSi12 specimens were carried out specimens produced with similar process parameters: as-built specimens and specimens manufactured with building platform heated to 200° and subjected to a similar annealing treatment (heating temperature of 240° C). In Ref.[15], the reduction of the tensile strength after annealing is limited (369 MPa for as-built and 361 MPa for heat treated), whereas in the present paper is larger (413 MPa in AB and 344 MPa). The difference could be due to the larger base platform temperature (200°C in Ref.[15] and 150°C in the present paper), which reduces the effect of the annealing treatment. Regarding the elongation to failure, the same trend is found in Ref.[15]: ε_f reduces after the heat treatment (4.38% in as-built and 4.05% after annealing) in Ref.[15], but the reduction is limited with respect to that found in the present paper (5.5% and 4.2%). The comparison with literature results confirms the decrement of the quasi static-mechanical properties with an annealing temperature of about 240 °C and highlights that a base platform heating above 150 °C reduces significantly the effect of the annealing temperature.

Vickers hardness within the cross-section was measured according to ISO 6507-1 Standard[34]. Hardness measurements were carried out on the cross-sections of four AB, four HT-320 and four HT-244 Gaussian specimens. For the location of the HV measuring points, the reader can refer to Reference[24, 27]. Fig. 2 compares the 95% confidence interval plot of the Vickers hardness measured on the SLM AlSi10Mg specimens in the three tested conditions.
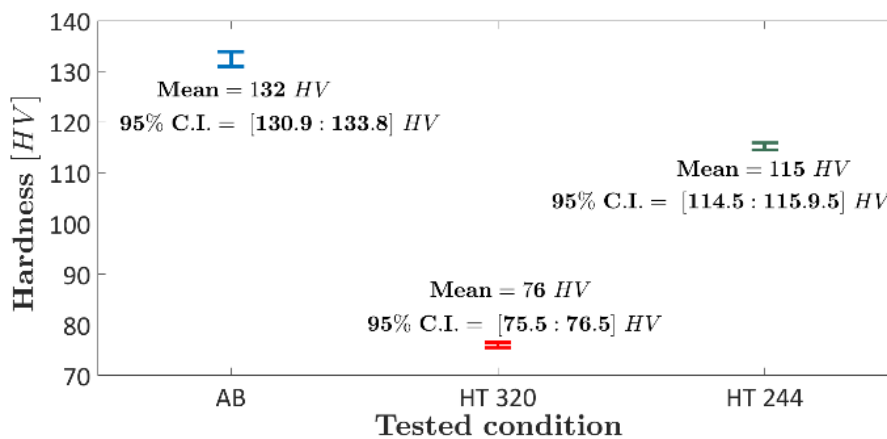

Figure 2: 95% confidence interval plot.

According to Fig. 2, the mean hardness of AB specimens is equal to 132 HV, whereas it reduces after the annealing heat treatment, being equal to 76 HV (42% variation) for the HT-320 specimens and 115 HV (13% variation) for the HT-244 specimens. On the contrary, the scatter is slightly reduced after the heat

treatments: the 95% confidence interval range of the measured HV values was $\pm$ 0.5 HV in both the HT-320 and the HT-244, whereas was $\pm$ 1.1 HV in the AB specimens.

The reduction of the mechanical strength in HT-320 specimens was mainly due to the coarsening of the microstructure and to the rupture of the fine Si network, characteristic of AB parts, with reinforcing precipitates such as the coherent β'' phase becoming less effective in obstructing the motion of the dislocations. On the contrary, due to the Si spheroidization ductility is strongly improved. On the other hand, HT-244 specimens retained higher strength and hardness thanks to the Si network being still intact after the treatment.

2.3 VHCF tests: test setup

Ultrasonic fatigue tests were carried out on Gaussian specimens with a large risk-volume of 2300 mm^3. The risk-volume is defined in Ref.[35, 36] as the volume of material subjected to a stress amplitude larger than the 90% of the maximum applied stress and corresponds to the region of material where the stress amplitude is large enough to originate a fatigue failure. When dealing with the VHCF response of AM parts, the defect size distribution must be accurately estimated from the experimental results[8, 12, 37] for a proper assessment of the HCF and of the VHCF response. Due to the significant influence of size-effect in VHCF[21, 36, 38], tests on large risk-volumes permit therefore to more reliably estimate the defect size distribution and, accordingly, to more properly compare the VHCF response[39].

Before running the ultrasonic tests, specimens were polished with sandpaper with increasing grit (mesh from 240 to 1000) in order to smooth the external surface and to prevent crack nucleation from large superficial scratches, with the aim of investigating the role of manufacturing defects (e.g., pores, defects due to incomplete fusion or due to improper bonding between layers) on the VHCF response, rather than the effect of the surface roughness. Indeed, large superficial scratches are large defects (similar to machining scratches) from which the fatigue crack starts to propagate immediately, with a number of cycle to failure smaller than 10^4 cycles. For failures below 10^4 cycles, the applied stress amplitude during the ultrasonic fatigue tests cannot be properly controlled due to the large loading frequency (i.e., the number of cycles below the selected stress amplitude during the transient phase is too high). Therefore, for investigating the effect of these types of defect on the fatigue response, High Cycle Fatigue tests with conventional testing machines are more appropriate. The machining of the specimens to the final shape is more appropriate to investigate the role of internal defects[19] but, since it removes a larger layer of material, it does not permit a proper assessment of the influence of surface and sub-surface defects which originate during the manufacturing process.

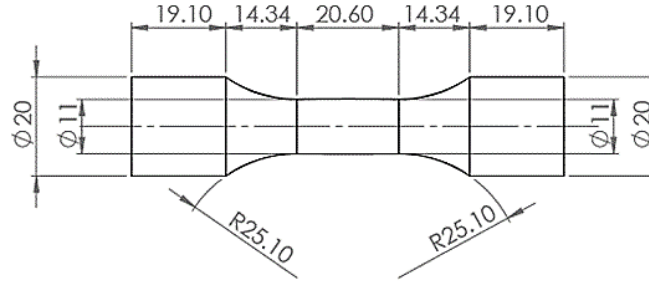The geometry of the tested Gaussian specimens is shown in Fig.3.

Figure 3: Geometry of the tested Gaussian specimens.

Fully-reversed constant stress amplitude tension-compression tests at a loading frequency of 20 kHz were carried out up to failure or up to 10^9 cycles (run-out number of cycles) by using the ultrasonic testing equipment available at Dynlab in Politecnico di Torino[18]. The applied stress amplitude at the specimen center, s_{center}, was kept constant during the tests through a feedback control based on the stress amplitude, s_{horn}, obtained from the strain measured with a strain gage (control gage) bonded to the horn. The dynamic elastic modulus measured with the Impulse Excitation Technique (IET) was adopted to evaluate s_{horn} and s_{center} from the measured strains. A calibration procedure was repeated on three AB, two HT-320 and three HT-244 specimens to correlate s_{center} and s_{horn}: in particular, a second strain gage (calibration gage) was bonded at the centre of the Gaussian specimens used for the calibration process. For the remaining specimens, an average linear correlation between s_{center} and s_{horn} was estimated from the calibration tests.

Fig. 4a shows the horn and the specimens (horn and specimens) with the *control gage* and the *calibration gage*. Fig. 4b shows the range of variation of s_{center} in the calibration procedure. In particular, for each acquired average value of s_{center} (average between all the acquired values, $s_{center,m}$), the ratio $s_{center}/s_{center,m}$ is shown.
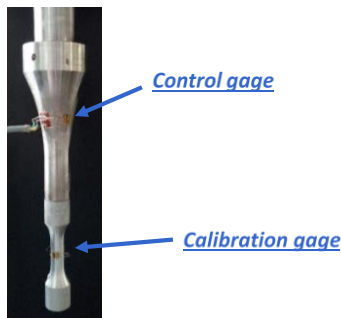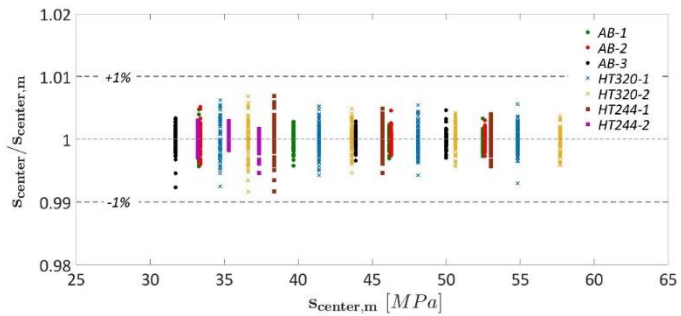
(a)   (b)

Figure 4: Calibration process: a) horn and specimens with the control and the calibration gage; b) Stress variation with respect to the average value.

9

According to Fig. 4b, the range of variation of s_{center} was within ± 1%, thus confirming that the uncertainty in the applied stress amplitude is very limited. Moreover, a load histogram was acquired during the tests: more than 99% of the cycles to failure was in the range $\pm\,1$ MPa (with respect to the selected stress amplitude), thus confirming the effectiveness of the developed control system.

Tests were carried out in continuous mode. The specimen self-heating[40] was kept under control by limiting the temperature below 25 °C with two vortex tubes[39]. During the test, the temperature was continuously measured at the specimen center with an OPTRIS CT-LT-15 infrared sensor. In particular, the inlet pressure of the vortex tube and the air flow were adjusted to maintain the temperature constant during the test. The uniformity of the temperature distribution within the large risk-volumes was also verified through Finite Element Analysis (FEA) in Ref.[41].

3. VHCF TEST RESULTS

In Subsection 3.1 the S-N plot of the experimental dataset is reported. In Subsection 3.2 fracture surfaces are analyzed. In the following, the defect from which the fatigue crack starts propagating will be called "critical defect".

3.1. S-N plot

Ultrasonic tests were carried out at s_{center} in the range 60 MPa and 95 MPa. Totally, 36 VHCF tests were carried out, with 23 failures and 13 runouts. 3 specimens (2 for AB and 1 for HT-320) failed before 10^4 cycles due to large surface scratches (Section 3.2); since it was not possible to properly control the applied stress amplitude, they were not considered for the estimation of the P-S-N curves.

All the fatigue failures originated from different types of defects present within the material (Subsection 4.2). In the following, the stress amplitude at the defect originating failure location (s_{local}, assessed through FEA) is considered for the analysis of the experimental data[22]. The S-N plot of the experimental dataset (s_{local} with respect to the number of cycles to failure, N_f) is shown in Fig. 5.
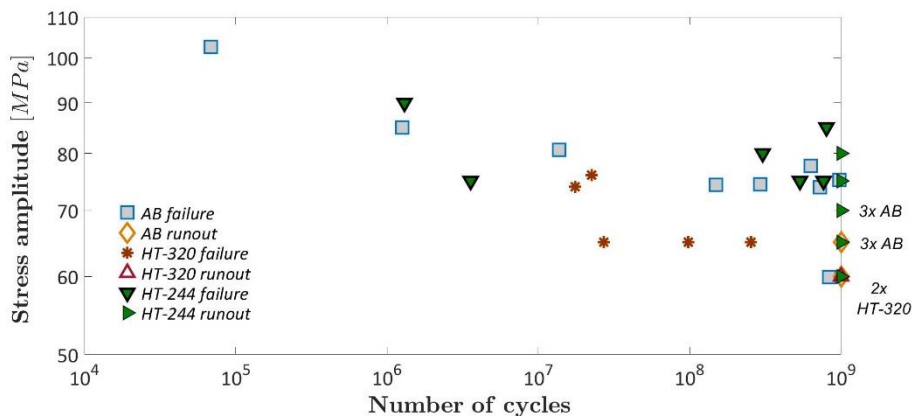
According to Fig. 5, HT-320 specimens showed the smallest VHCF strength, whereas HT-244 specimens were characterized by the largest VHCF strength. The largest runout stress amplitude in HT-244 specimens occurred at 80 MPa, whereas it was equal to 65 MPa for the AB specimens and to 60 MPa for the HT-320 specimens. The scatter of the experimental failure was large, due to the random size of the defects originating failure. In the following Sections the defects originating failure will be analysed and the effect of the annealing temperature on the VHCF response will be investigated in a statistical framework by considering the conditional P-S-N curves.

The experimental results are in agreement with those reported in the literature. For the AlSi12 specimens tested in Ref.[15], the stress relief treatment on specimens produced with base platform heating does not significantly affect the fatigue response. Indeed, as for the quasi-static test, the platform is heated to a temperature close to the annealing temperature (200°C), thus minimizing the effect of the stress relief treatment. Accordingly, experimental results in Ref.[18] confirm that the effect of a stress relief treatment is maximized (i.e., if microstructural changes are not detrimental[24]) for specimens produced without heating the building platform. In Ref.[42] experimental tests are carried out on AlSi10Mg specimens obtained by heating the building platform to 200°C: since it was demonstrated in Ref.[15] that the effect of the annealing treatment is negligible if the building platform is heated to a temperature close to the annealing temperature, experimental results in Ref.[42] can be considered for the comparison. In Ref.[42] the runout limit at 10^8 cycles is equal to 90 MPa, whereas in the present paper failures at stress amplitude smaller than 90 MPa are found (i.e., the runout limit is equal to 75 MPa). The difference could be mainly due to the specimen conditions: in Ref.[42], the VHCF tests were carried out on hourglass specimens with small-risk volumes manufactured in vertical direction. The specimens were also machined to the final shape after the AM process. The machining process, the size-effect and the building orientation (i.e., in horizontal Gaussian specimens almost all the fatigue failures located close to the removed supports) can contribute to the reduction of the VHCF strength found in the present paper.

3.2. Fracture surfaces

Fracture surfaces were analysed with the optical microscope (Leica Z16 APO A) and with the Scanning Electron Microscope (SEM). Figure 6 shows the two types of fracture surfaces found experimentally and two cross-sections of a fracture surface. Fig. 6a shows an example of failure originated from a large superficial scratch in the support area (premature failure) and Figure 6b shows a typical fracture surface of a VHCF failure originating from a defect close the specimen surface. Fig. 6c and Fig. 6d show the cross-sections of a fracture surface of an AB specimen in the crack propagation region and in the final failure region, respectively.
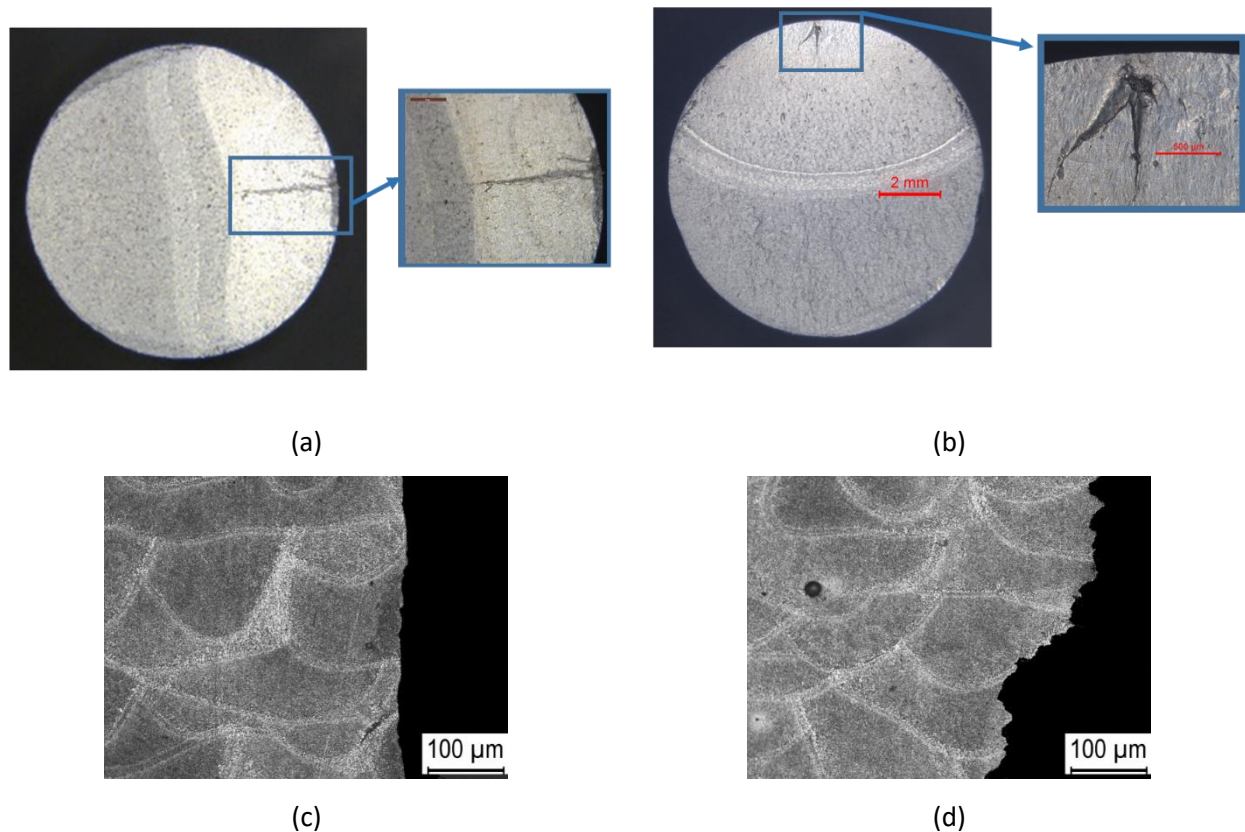
Figure 6: Fracture surfaces and crack propagation analysis: a) premature failure due to a large superficial scratch; b) VHCF failure from a sub-surface defect; c) crack propagation zone in AB specimen; d) final failure zone in AB specimen.

In Fig. 6a, the large superficial scratch in the region where building supports were removed is clearly visible, with the fatigue crack propagating immediately with a Stress Intensity Factor (SIF) larger than the threshold for crack propagation, thus originating a premature fatigue failure (Section 3.1). In Fig. 6b, a typical fracture surface of a failure originating from a sub-surface defect is shown. Failures originating from sub-surface defects will be investigated in detail in the following Sections.

Regarding the crack propagation analysis (Figs. 6c and 6d), it may be appreciated that the crack propagates linearly in the first case, crossing melt pools and, likely, grain boundaries without being deviated. On the contrary, in the final failure region the crack follows a more irregular path. It is evident that detachment often occurs along the heat affected zone which, due to its coarser microstructure, exhibits lower resistance. The same behaviour in both areas was also exhibited by HT-320 and HT-244 specimens, regardless of the different microstructure induced by the heat treatments.

4. INFLUENCE OF DEFECTS AND OF THE ANNEALING TEMPERATURE: DISCUSSION

In Section 4 the effect of defects and of the annealing temperature on the VHCF is assessed. In Subsection 4.1 defects originating the fatigue crack (type, morphology and size) are compared. In Subsection 4.2 the

12

Stress Intensity Factor (SIF) threshold, k_{th}, is analyzed. In Subsection 4.3 the conditional P-S-N curves are compared.

4.1. Defect distribution: location, type and size

Fig. 7 shows the distribution of critical defects within the specimen cross section; the coordinate axes report the locations of the defects along the x and y direction, normalized by the specimen radius at the failure longitudinal coordinate.
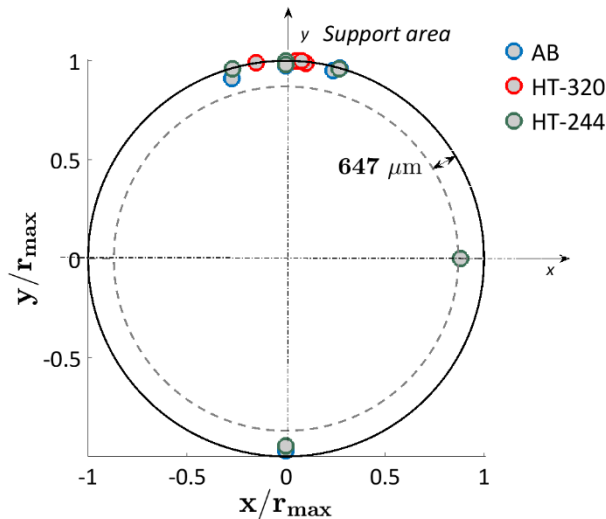

Figure 7: Location of critical defects within the cross-section.

According to Fig. 7, defects originating failure are mainly concentrated close to the specimen surfaces, in a region of material with radial size of 647 µm. In particular, 17 out of 20 specimens were in the region where support structure were removed, thus highlighting the detrimental effect of the mechanical removal of supports on the VHCF response. A removal of a layer of material of at least 1 mm through a machining process would avoid nucleation from dangerous superficial defects and would probably enhance the VHCF response. On the other hand, Fig. 7 confirms that a manual polishing process is effective in limiting crack nucleation from large superficial scratches due to high surface roughness (only 3 out of 23 specimens showed premature failures) and permits to properly investigate the influence of internal defects on the VHCF response, which is the objective of this paper.

A more detailed analysis of the critical defects was carried out with the SEM. Three types of defects originated the fatigue failure in all the tested specimens (Fig. 8): pores and cluster of pores (Fig. 8a); surface defects probably originating during the removal of the support structures (Fig. 8b); incomplete fusion defect (Fig. 8c).

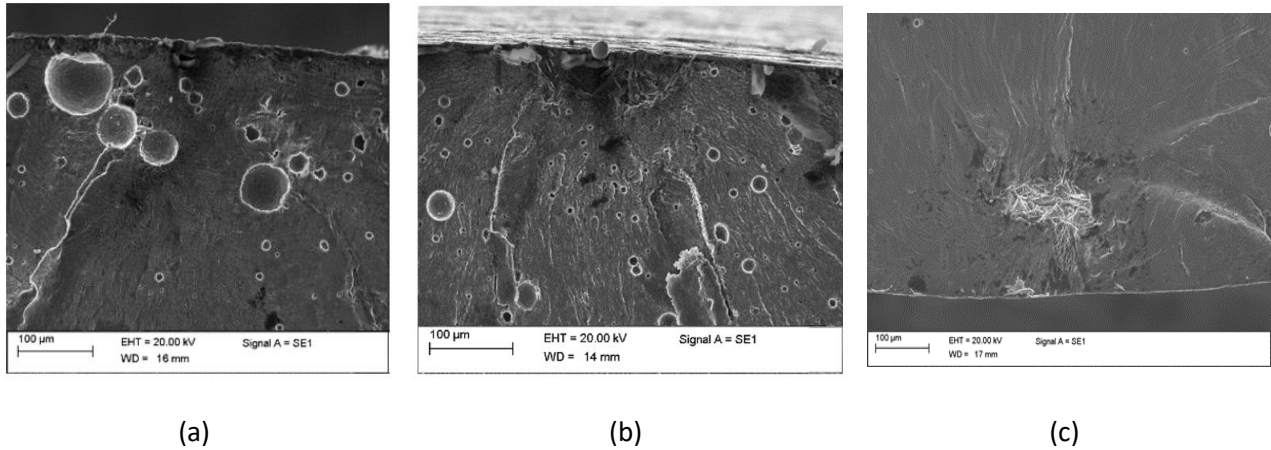(a)   (b)   (c)

Figure 8: Types of critical defects: a) cluster of pores (HT-320); b) defect originating during the removal of support structures (AB); c) defect originating due to an incomplete fusion (HT-244).

Fig. 9 shows the histogram of the defect types for AB, HT-320 and HT-244 specimens. In AB and HT-320 specimens, pores are in general the most detrimental defects and originate the fatigue crack in the 67% and 80% cases, respectively. About 20% of the fatigue failures initiates from surface defects formed probably when the support structures were mechanically removed in AB and HT-320 specimens, whereas defects due to an incomplete fusion were not found in HT-320 specimens and were less frequent in AB specimens (1 out 9, 11%). On the contrary, they originated the fatigue failures in all the tested HT-244 specimens, with no fatigue failure originating from other types of defects.

It has been reported in literature that heat treatments generally do not affect the dimensions of pores [43-46] as well as of incomplete fusion defects. Therefore, the evident variations among the populations of critical defects in specimens subjected to different heat treatments shall not be ascribed to a real change in number and type of defects present in the specimens, but rather to a change in the conditions necessary for the critical propagation of a crack.
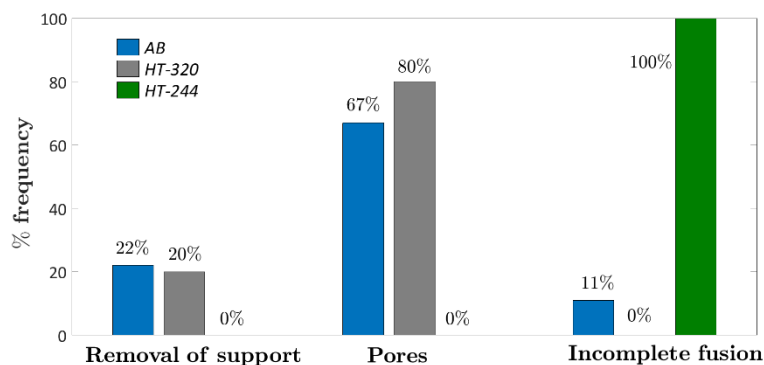

Figure 9: Histogram of the critical defect types.

The defect size was finally compared. The analysis of the defect type and morphology provides useful information on the process parameters that could be optimized to avoid their formation. On the other hand,

since the VHCF response is mainly driven by the defect size[35] rather than by the defect composition or morphology, the defect size must necessarily be considered to investigate the effect of defects on the VHCF response. Differently from defects typical of parts produced through traditional manufacturing processes, such as spherical inclusions which generally are characterized by a more regular shape[22], defects and impurities in AM parts show a more irregular morphology[37]. Defects with significantly different morphologies (or group of defects) can be compared by considering an equivalent defect size (or effective defect size, according to Ref.[37]) in place of the real defect size. The equivalent defect size corresponds to the size of a defect with regular boundaries with the same behaviour with respect to the crack initiation and propagation process and thus it permits to compare defects characterized by completely different morphologies.

For the defects found experimentally and for group of defects, the equivalent defect size, $\sqrt{a_c}$, was estimated according to Ref.[12, 37]. Table 3 compares the $\sqrt{a_c}$ in the AlSi10Mg specimens in the three investigated conditions: for each defect type and specimen condition, the minimum value, $\sqrt{a_{c,min}}$, and the maximum value, $\sqrt{a_{c,max}}$, are reported.

	$\sqrt{a_{c,min}}$ [μm]	$\sqrt{a_{c,max}}$ [μm]
All defects		
_AB_	103	198
_HT-320_	86	160
_HT-244_	133	365
Pores		
_AB_	103	174
_HT-320_	86	160
_HT-244_	/	/
Removal of supports		
_AB_	116	198
_HT-320_	102	102
_HT-244_	/	/
Incomplete fusion		
_AB_	195	195
_HT-320_	/	/
_HT-244_	133	365

Table 3: Size of critical defects in AB, in HT-320 and in HT-244 specimens.

According to Table 3, defects in AB and in HT-244 specimens are within a larger range ([103: 198] μm for AB and [133: 365] μm for HT-244); whereas the range is reduced for HT-320 specimens ([86: 160] μm). The difference in the defect size range is reduced if the same types of defects are compared. If only pores are taken into account, the range found in the AB and in the HT-320 is very close and the difference is reduced, in agreement with literature results showing that low temperature heat treatments do not alter the pore size[45, 46].

The defect size can also be compared with the Statistics of Extreme Values. According to Ref.[35], the critical defect follows the Largest Extreme Value Distribution (LEVD). Due to the small number of failure data, the LEVD of the defect size for each tested condition was not estimated. On the other hand, by considering that low temperature heat treatments do not alter the pore size[45, 46], the LEVDs for all critical pores and incomplete fusion defects were estimated for comparison purposes. Fig. 10 shows the Gumbel plot of pores and incomplete fusion defects, together with the estimated LEVD distributions.
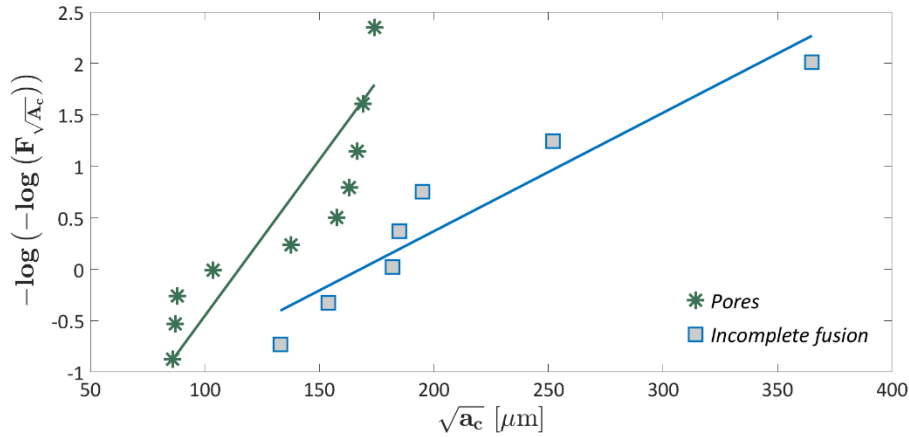

Figure 10: Gumbel plot comparing the LEVD for pores and incomplete fusion defects.

The Gumbel plot confirms that pores and defects due to an incomplete fusion follow two different LEVDs, with the latter characterized by a larger size, in agreement with Ref.[47]. The LEVD well describes the distribution of the defects due to an incomplete fusion, whereas the fit for the distribution of pores is worse. A possible explanation can be related to the fact that both single pores and cluster of pores (with different number of pores) were considered for estimating the pore distribution. It is therefore possible that single pores and cluster of pores follows two slightly different distributions, thus justifying that the LEVD does not fit well the experimental data. However, Fig. 10 clearly highlights that defects due to incomplete fusion were characterized by larger size, with 5 out 7 defects characterized by $\sqrt{a_c}$ larger than the largest pore size found experimentally.

4.2. K_{th} trend

The Stress Intensity Factor threshold, K_{th}, provides information about the material resistance to crack initiation. Moreover, according to Ref.[7], the large scatter typical of fatigue results of tests on AM parts can be reduced by considering the SIF threshold, which can be therefore reliably employed for designing AM parts[48]. A general linear model ($k_{th} = c_{th}(HV + 120)\sqrt{a_c}$, being c_{th} a constant coefficient) was considered for interpolating the SIF threshold trend with respect to $\sqrt{a_c}$ (Ref.[27, 49]).

According to Ref.[48], the SIF computed by considering the measured $\sqrt{a_c}$ equals the SIF threshold if the fatigue failure occurs at a N_f above the so-called "knee point" (i.e., below the knee-point the SIF associated to the initial defect is larger than the SIF threshold). In Ref.[48] the knee-point is assumed to be equal to $1 \cdot 10^6$ cycles. In this paper it is conservatively considered equal to $2 \cdot 10^6$ cycles: failures occurred at N_f below $2 \cdot 10^6$ were therefore not considered.

Fig. 11 shows the SIF threshold with respect to $\sqrt{a_c}$ in a log-log plot. In order to take into account the different Vickers hardness in the three investigated conditions, the SIF threshold is normalized with respect to the factor $c_{th} \cdot (HV + 120)$. The estimated median curve, the 5-th and the 95-th quantiles are shown in the Figure, together with the normalized experimental data.
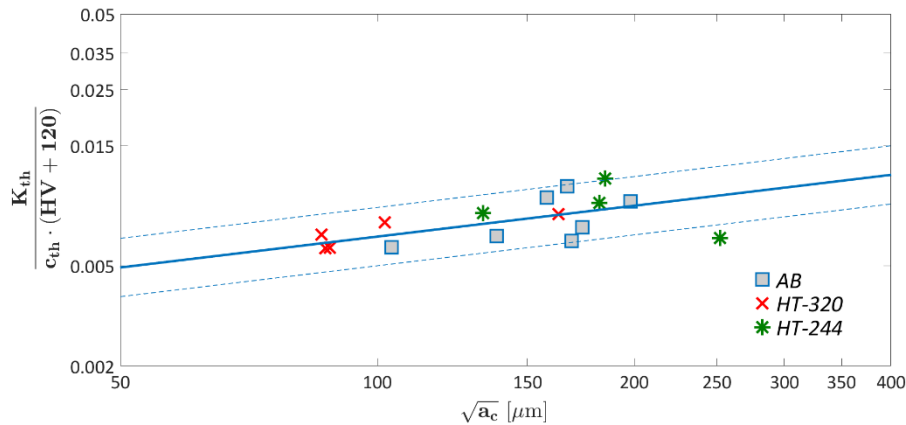

Figure 11: Normalized K_{th}, with respect to $\sqrt{a_c}$.

According to Fig. 11, the normalized SIF threshold follows a linear trend, in agreement with literature results[8], with only two data outside the 90% estimated confidence interval. The slope of the interpolating function is equal to 0.5 and close to the values reported in Ref.[8] (between $1/3$ and $1/2$). The model shown in Fig. 11 can be conservatively used to design AM components, provided that the critical defect in the risk-volume of the component can be experimentally measured (e.g., through micro-CT scan) or properly predicted (e.g., through the Statistic of Extreme Values). If the HV of each investigated working condition is taken into account, the specimens subjected to the heat treatment at 320 °C show the smallest SIF threshold; on the contrary AB and HT-244 specimens are characterized by a similar resistance to crack initiation. The effect of other factors on the VHCF response, such as the residual stresses, will be discussed in the following Section.

4.3 Conditional P-S-N curves

In this Section, the conditional P-S-N curves (i.e., conditioned to the equivalent defect size $\sqrt{a_c}$) are estimated according to the model proposed in Ref.[49, 50] and compared. The logarithm of the fatigue life was assumed to follow a Normal distribution, with mean linearly dependent on the applied stress amplitude and on the critical defect size and constant standard deviation. Runout specimens were also taken into account: the size of the critical defect in runout specimens was computed by considering the 1-th quantile of the normalized K_{th} shown in Fig. 11 and the corresponding runout stress amplitude. It is worth to note that the conditional P-S-N curves are conditioned to the equivalent defect size (and not to the actual defect size), regardless of the defect composition or a morphology. Therefore, the conditional P-S-N curves can be employed for each type of defect that is present within the AM part or that can be reliably estimated or predicted.

In Fig. 12 the conditional P-S-N for the specimens in the three investigated working conditions are reported: the median, the 5-th quantile and the 95-th quantiles are shown. Fig. 12a shows the P-S-N for AB specimens and for $\sqrt{a_c} = 167$ μm (median defect size in AB specimens); Fig. 12b shows the P-S-N shows for HT-320 specimens and for $\sqrt{a_c} = 88$ μm (median defect size in HT-320 specimens); Fig. 12c shows the P-S-N shows for HT-244 specimens and for $\sqrt{a_c} = 183$ μm (median defect size in HT-244 specimens). The VHCF failure originating from the defect (or the two closest defects) with size corresponding to the median size is highlighted in the figure (thicker marker).
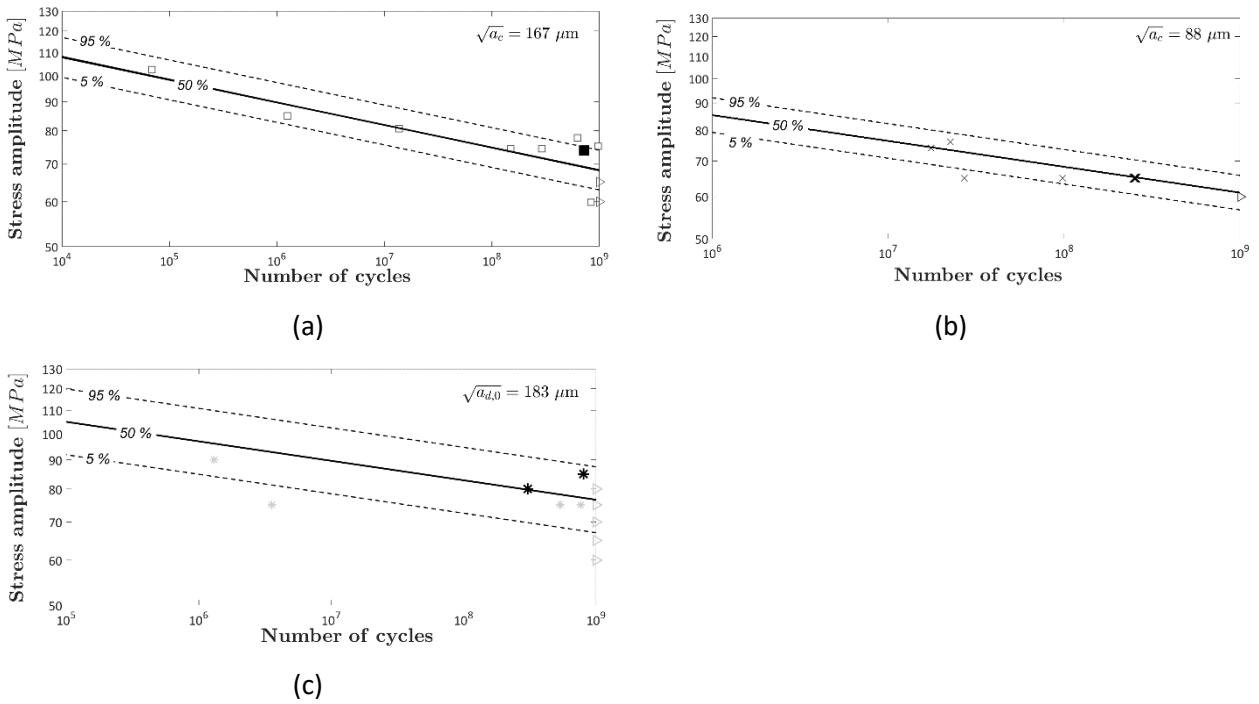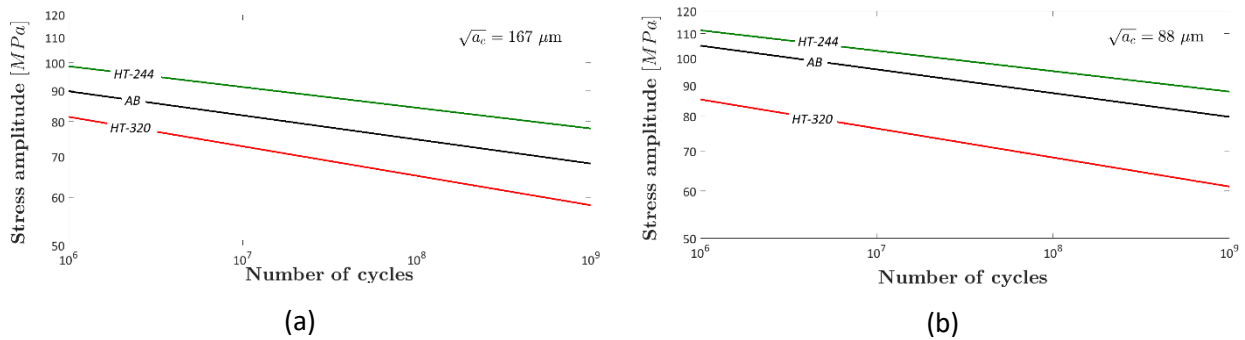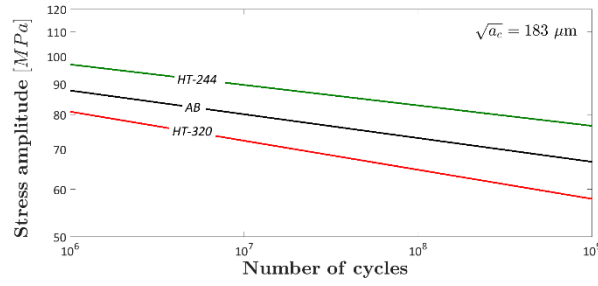

(a)

(b)

(c)

Figure 12: Conditional P-S-N curves relative to the median $\sqrt{a_c}$ for each specimen type: a) AB specimens; b) HT-320 specimens; c) HT-244 specimens.

According to Fig. 12, the model considered for the estimation of the P-S-N curves well fits the experimental results. In particular, the fatigue failures originating from the defect with $\sqrt{a_c}$ corresponding to the median defect size is within the 90% confidence interval for the three investigated conditions. The estimated P-S-N curves, therefore, can be reliably considered for comparing the VHCF lives.

Fig. 13 compares the median conditional P-S-N curves estimated for $\sqrt{a_c}$ corresponding to the median defect size for each specimen type: Fig. 13a for $\sqrt{a_c} = 167$ μm (median defect size for AB specimens); Fig. 13b for $\sqrt{a_c} = 88$ μm (median defect size for HT-320 specimens); Fig. 15c for $\sqrt{a_c} = 183$ μm (median defect size for HT-244 specimens). Moreover, in order to take into account the scatter associated to the experimental failures and to more properly highlight the effect of the HT-244 with respect to the as-built condition, the VHCF strength of AB and HT-244 at a reference number of cycles, N_{ref}, of $5 \cdot 10^8$ was compared. In particular, according to a statistical procedure based on the fatigue life distribution, all the experimental failures were gathered together at N_{ref}, in order to estimate the VHCF strength (corrected VHCF strength, s_{corr}) at N_{ref} and for a selected defect size. For more details on the procedure for the estimation of the distribution of s_{corr}, the reader is referred to Ref.[22, 24, 27]. Fig. 13d compares the probability density function, $p(s_{corr})$, of the corrected VHCF strength at $5 \cdot 10^8$ cycles for a defect size corresponding to the median size of each tested condition (i.e., AB and HT-244); Fig. 13e compares the $p(s_{corr})$ estimated at $5 \cdot 10^8$ cycles for a defect size of 365 μm, corresponding to the largest defect found. The two-sided 90-th confidence intervals are also shown in Fig. 13. As highlighted in the previous Sections, the defect size is not affected by the heat treatment. According to the LEVD, rare defects with $\sqrt{a_c}$ larger than the highest found for a specific testing condition are possible, especially in real components characterized by large risk-volumes. For this reason, the P-S-N curves and the probability density function were estimated also for $\sqrt{a_c}$ larger than the largest found experimentally for a particular testing condition (e.g., P-S-N curve for HT-320 at $\sqrt{a_c} = 183$ μm even if the largest $\sqrt{a_c}$ is equal to 160 μm).

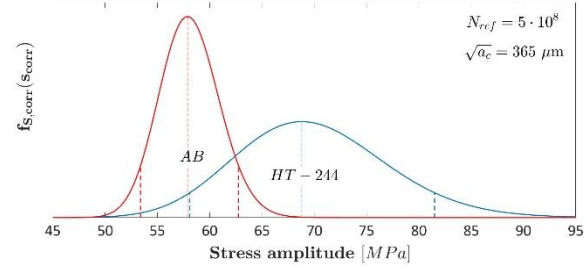(a)   (b)

(c)
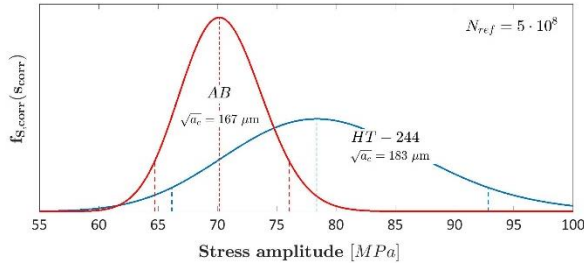
(d)

(e)

Figure 13: Median conditional P-S-N curves for $\sqrt{a_c}$ corresponding to the median $\sqrt{a_c}$ for each specimen type: a) $\sqrt{a_c} = 167$ μm (AB specimen); b) $\sqrt{a_c} = 88$ μm (HT-320 specimen); c) $\sqrt{a_c} = 183$ μm (HT-244 specimen); d) $p(s_{corr})$ of AB and HT-320 for $\sqrt{a_c}$ corresponding to the median defect size at $5 \cdot 10^8$ cycles; e) $p(s_{corr})$ of AB and HT-320 for $\sqrt{a_c} = 365\ \mu m$ at $5 \cdot 10^8$ cycles.

According to Fig. 13, HT-320 has a negative effect on the VHCF response. In particular, the curve for the HT-320 specimens is always below the curve for AB specimens. Indeed, as expected from the significant reduction of the hardness (Fig. 2), the rupture and the spheroidization of the Si network induced by annealing at 320 °C has a negative effect on the VHCF life. Residual stresses should also be analyzed: all the specimens were produced with the build platform heated to 150°C, thus limiting the residual stresses to a minimum value close to 8 MPa[13]. Even if the suggested heat treatment permits to further minimize the residual stresses, the effect of the microstructural changes is prevalent. On the contrary, the VHCF response is enhanced through the HT-244 : the P-S-N curves for the optimized HT-244 specimens lay always above the curve for AB specimens. The difference increases with $\sqrt{a_c}$, showing an improved resistance to large defects with respect to AB specimens. Therefore, the optimization of the annealing temperature proved to be effective: the HT-244 does not alter the original microstructure[24] and it minimizes the detrimental effects of the surface residual stresses, thus justifying the more frequent crack initiation from internal and larger defects due to an incomplete fusion (i.e., in AB specimens crack starts more frequently from smaller pores close to the surface where the residual stresses reach the maximum value[15]). The results obtained by comparing the P-S-N curves are confirmed by considering the VHCF strength distribution shown in Fig. 13d and 13e and, in particular, the VHCF strength at 5% failure probability, which is more indicated in case of limited number of tested specimens. For the median defect size of each tested condition (Fig. 13d) the

20

influence of the heat treatment is evident by considering the mean value of the distribution. On the other hand, the 5% quantile of s_{corr} for the HT-244, due to the scatter of the experimental data, is close to the median value for the as-built specimens. The beneficial effect of the HT-244 is more evident for larger defect sizes: for $\sqrt{a_c} = 365$ µm, the 5% quantile of the HT-244 is above the median value of AB. The P-S-N curves and the probability density function confirm that the HT-244 is more effective for large $\sqrt{a_c}$: indeed, by considering the VHCF strength, the difference between the AB and the HT-244 increases as the $\sqrt{a_c}$ increases. This is a further confirmation of the importance of heat treatments or, in general, post treatments. Indeed, even if defects control the VHCF response and heat treatments do not affect the defect size, they can be effective in reducing the sensitivity to defects of AM parts (e.g., they help minimizing residual stresses and strengthening the microstructure).

In conclusion, heat treatments for AM parts should be experimentally validated and optimized before being employed for components in service conditions. Microstructural changes induced by HT-320 are detrimental, making the relief of residual stresses less effective. On the contrary, the HT-244 does not alter the microstructure and the relief of residual stresses has a clear effect that finally permits to enhance the VHCF response, especially for large and rare defects which can be originated during the manufacturing process.

5. CONCLUSIONS

In the paper, the influence of the annealing temperature on the Very-High-Cycle-Fatigue (VHCF) of an SLM AlSi10Mg alloy was investigated. Ultrasonic VHCF tests up to 10^9 cycles were carried out on Gaussian specimens with large risk-volumes in three conditions: as-built, subjected to a heat treatment suggested by the system supplier (2 hours heating to 320 °C and air cooling to room temperature) and subjected to an heat treatment proposed by the authors (2 hours heating to 244 °C and air cooling to room temperature, HT-244). The microstructure and the mechanical properties obtained after the investigated heat treatments were compared with those experimentally assessed on as-built specimens. The main conclusions can be summarized as follows:

1) An annealing temperature of $320°C$ induces the spheroidization of the Si network, thus giving rise to reduced quasi-static mechanical strength but much improved ductility. On the other hand, annealing at $244°C$ allowed to retain the Si network intact and permitted to obtain a balanced set of mechanical properties: acceptable levels of strength and elongation to failure together with an effective stress relief were finally obtained.

2) Critical defects were mainly concentrated near the surface (largest radial distance equal to 647 µm). Pores and cluster of pores were the most frequent defects in as-built specimens and in the specimens subjected to the heat treatment suggested by the supplier, with the other types of defects less frequent. On the other hand, defects due to an incomplete fusion, which were characterized by a

21

larger size, originated the fatigue failure in all the specimens subjected to the heat treatment proposed by the authors.

3) An annealing temperature of 244° C permitted to enhance the VHCF response. The median P-S-N curve for the specimens subjected to the heat treatment proposed by the Authors was above the P-S-N curves for the as-built specimens; on the other hand, the annealing temperature suggested by the producer of the AM equipment had a negative influence on the VHCF response. As expected, the rupture and the spheroidization of the Si network, which were induced by the heat treatment suggested by the supplier, induced a decrement of the VHCF strength with respect to the non-annealed condition. The reduction of the residual stresses had no effect, since the effect of microstructural changes was prevalent. On the other hand, an annealing temperature of 244 °C permitted to obtain a microstructure close to the microstructure of the as-built specimens and, at the same time, to minimize residual stresses, thus improving the fatigue behaviour.

4) The minimization of the residual stresses may be ineffective if the microstructural modifications induced by the heat treatment are not taken under control and experimentally validated.

REFERENCES

1 Lewandowski, J.J., Seifi, M. Metal Additive Manufacturing: A Review of Mechanical Properties. *Annual Review of Materials Research* 2016; **46:1**: 151-186.

2 Yadollahi, A., Shamsaei, N. Additive manufacturing of fatigue resistant materials: Challenges and opportunities. *Int. J. Fatigue* 2017; **98**: 14-31

3 Mower, T.M., Long, M.J. Mechanical behavior of additive manufactured, powder-bed laser-fused materials. *Mater. Sci. Eng. A* 2016; **651**: 198–213.

4 Uzan, N.E., Shneck, R., Yeheskel, O., Frage, N. Fatigue of AlSi10Mg specimens fabricated by additive manufacturing selective laser melting (AM-SLM). *Mater. Sci. Eng. A* 2017; **704**: 229–237.

5 Edwards, P., Ramulu, M. Fatigue performance evaluation of selective laser melted Ti–6Al–4V. *Mater. Sci. Eng. A* 2014; **598**: 327–337.

6 Aboulkhair, N.T., Maskery, I., Tuck, C., Ashcroft, I., Everitt, N.M. Improving the fatigue behaviour of a selectively laser melted aluminium alloy: Influence of heat treatment and surface quality. *Mater. Design.* 2016; **104**: 174–182.

7 Yadollahi A, Mahtabi MJ, Khalili A, Doude HR, Newman JC Jr. Fatigue life prediction of additively manufactured material: Effects of surface roughness, defect size, and shape. *Fatigue Fract. Eng. Mater. Struct.*, 2018;**41**:1602–1614.

8 Beretta, S., Romano, S. A comparison of fatigue strength sensitivity to defects for materials manufactured by AM or traditional processes. *Int. J. Fatigue*. 2017; **94**: 178-191.

9 Tang, M., Pistorius, P.C. Oxides, porosity and fatigue performance of AlSi10Mg parts produced by selective laser melting. *Int. J. Fatigue*. 2017; **94**: 192-201.

10 Beevers, E., Brandão, A.D., Gumpinger, J., Gschweitl, M., Seyfertc, C., Hofbauer, P., Rohr, T., Ghidini, T. Fatigue properties and material characteristics of additively manufacturedAlSi10Mg–Effect of the contour parameter on the microstructure, density, residual stress, roughness and mechanical properties. *Int. J. Fatigue* 2018; **117**: 148-162.

11 Bauereiß, A., Scharowsky, T., Körner, C. Defect generation and propagation mechanism during additive manufacturing by selective beam melting. *J Mater Process Tech* 2014; **214**: 2522-2528.

12 Masuo, H., Tanaka, Y., Morokoshi, S., Yagura, H., Uchida, T., Yamamoto, Y., Murakami, Y. Influence of defects, surface roughness and HIP on the fatigue strength of Ti-6Al-4V manufactured by additive manufacturing. *Int. J. Fatigue* 2018; **117**: 163-179.

13 Fergani, O., Wold, A.B., Berto, F., Brotan, V., Bambach, M. Study of the effect of heat treatment on fatigue crack growth behaviour of 316L stainless steel produced by selective laser melting. *Fatigue Fract. Eng. Mater. Struct.*, 2018;**41**:1102–1119.

14 Brandl, E., Heckenberge, U., Holzinger, V., Buchbinder, D. Additive manufactured AlSi10Mg samples using Selective Laser Melting (SLM): Microstructure, high cycle fatigue, and fracture behaviour. *Mater. Design.* 2012; **34**: 159–169.

15 Siddique, S., Imran, M., Wycisk, E., Emmelmann, C., Walther, F. Influence of process-induced microstructure and imperfections on mechanical properties of AlSi12 processed by selective laser melting. *J. Mater. Process. Technol.* 2015; **221**: 205–213.

16 Maskery, I., Aboulkhair, N.T., Tuck, C., Wildman, R.D., Ashcroft, I.A., Everitt, N.M., Hague, R.J.M. Fatigue performance enhancement of selectively laser melted aluminium alloy by heat treatment. *Solid Free. Fabr. Symp.* 2015: 1017–1025.

17 Wycisk, E., Siddique, S., Herzog, D., Walther, F., Emmelmann, C. Fatigue Performance of Laser Additive Manufactured Ti–6Al–4V in Very High Cycle Fatigue Regime up to 109 Cycles. *Frontiers in Materials*. 2015; **2 (72)**: 1-8.

18 Siddique, S.,Imran, M., Walther, F. Very high cycle fatigue and fatigue crack propagation behavior of selective laser melted AlSi12 alloy. *Int. J. Fatigue 2017*; **94**: 246-254..

19 Günther, J., Krewerth, D., Lippmann, T., Leuders, S., Tröster, T., Weidner, A., Biermann, H, Niendorf, T. Fatigue life of additively manufactured Ti–6Al–4V in the very high cycle fatigue regime. *Int. J. Fatigue* 2017; **94 Part 2**: 236-245.

20 Paolino, D.S., Rossetto, M., Chiandussi, G., Tridello, A. *Sviluppo di una macchina a ultrasuoni per prove di fatica gigaciclica*. Proceedings of the 41th AIAS Conference (2012), Vicenza, (In Italian).

21 Paolino, D.S., Tridello, A., Chiandussi, G., Rossetto, M. On specimen design for size effect evaluation in ultrasonic gigacycle fatigue testing. *Fatigue Fract. Engng. Mater. Struct.* 2014; **37**: 570–579.

22 Tridello, A. VHCF response of Gaussian specimens made of high-strength steels: comparison between unrefined and refined AISI H13. *Fatigue Fract. Engng. Mater. Struct. 2017;* **40** (Issue 10): 1676–1689.

23 Tridello, A., Paolino. D.S., Chiandussi, G., Rossetto, M. Comparison between dog-bone and Gaussian specimens for size effect evaluation in gigacycle fatigue. *Frattura e Integrità Strutturale* 2013; **26**: 49-56.

24 Tridello, A., Fiocchi, J., Biffi, C.A., Chiandussi, G., Rossetto, M., Tuissi, A., Paolino, D.S. VHCF response of Gaussian SLM AlSi10Mg specimens: Effect of a stress relief heat treatment. *Int. J. Fatigue* 2019; **124**: 435-443.

25 Renishaw plc. Laser Meting: Aluminum AlSi10Mg_25mm_AM250-400W Parameter Validation; 2014.

26 Fiocchi, J., Tuissi, A., Bassani, P., Biffi, C.A. Low temperature annealing dedicated to AlSi10Mg selective laser melting products. *J Alloy Compd* 2017; **695**: 3402–3409.

27 Tridello, A., Biffi, C.A., Fiocchi, J., Bassani, P., Chiandussi, G., Rossetto, M., Tuissi, A., Paolino, D.S. VHCF response of as-built SLM AlSi10Mg specimens with large loaded volume. *Fatigue Fract. Engng. Mater. Struct.* 2018; **41**: 1918–1928.

28 ISO/ASTM 52921:2013. Standard terminology for additive manufacturing – Coordinate systems and test methodologies. International Standard Organization (ISO), Genève; 2013

29 SLM Solutions Group AG, 3D metals: the range of our standard metal powders (2018), Lubeck.

30 Biffi, C.A., Fiocchi, J., Bassani, P., Paolino, D.S., Tridello, A., Chiandussi, G., Rossetto, M., Tuissi, A. Microstructure and preliminary fatigue analysis on AlSi10Mg samples manufactured by SLM. *Procedia Structural Integrity.* 2017*;* **7**: *50-57*.

31 Colombo, C., Biffi, C.A., Fiocchi, J., Tuissi, A., Vergani, L.M. Effect of optimized heat treatments on the tensile behavior and residual stresses of selective laser melted AlSi10Mg samples. *Key Eng. Mater.*2019; **813**: 364-369.

32 Salmi, A., Atzeni, E., Iuliano, L., Galati, M. Experimental analysis of residual stresses on AlSi10Mg parts produced by means of Selective Laser Melting (SLM), *Procedia CIRP* 2017; **62**: 458–463.

33 Aboulkhair, N.T., Maskery, I., Tuck, C., Ashcroft, I., Everitt, N.M. The microstructure and mechanical properties of selectively laser melted AlSi10Mg: the effect of a conventional T6-like heat treatment. *Mater Sci Eng A* 2016; **667**: 139–146.

34 EN ISO 6507-1 (2005) Metallic materials - Vickers hardness test - Part 1: Test method, International Standard Organization (ISO), Genève.

35 Murakami, Y. (2002) Metal Fatigue: Effects Of Small Defects And Nonmetallic Inclusions. Elsevier Ltd, Oxford, UK.

36 Furuya, Y. Notable size effects on very high cycle fatigue properties of high strength steel. *Mater. Sci. Eng. A.* 2011*;* **528**: 5234–5240.

37 Yamashita, Y., Murakami, T., Mihara, R., Okada, M., Murakami, Y. Defect Analysis and Fatigue Design Basis for Ni-based Superalloy 718 manufactured by Additive Manufacturing. *Procedia Structural Integrity* 2017; **7**: 11-18.

38 Tridello, A., Paolino, D.S., Chiandussi, G., Rossetto, M. VHCF response of AISI H13 steel: assessment of size effects through Gaussian specimens. *Procedia Eng.* 2015; **109**: 121–127.

39 Tridello, A., Paolino, D.S., Chiandussi, G., Rossetto, M. Effect of electroslag remelting on the VHCF response of an AISI H13 steel. *Fatigue Fract Eng Mater Struct* 2017; **40 (11)**: 1783–1794.

40 Tridello, A., Paolino, D.S., Chiandussi, G., Rossetto, M. Gaussian specimens for VHCF tests: Analytical prediction of damping effects, *Int. J. Fatigue*. 2016; **83**: 36-41.

41 Tridello, A., Paolino. D.S., Chiandussi, G., Rossetto, M. Gaussian Specimens for Gigacycle Fatigue Tests: Evaluation of Temperature Increment. *Key Eng. Mater.* 2015; **625**: 85–88.

42 Awd, M.; Siddique, S.; Johannsen, J.; Emmelmann, C.; Walther, F. Very high-cycle fatigue properties and microstructural damage mechanisms of selective laser melted AlSi10Mg alloy. *Int. J. Fatigue* 2019, **124**, 55–69.

43 Girelli, L., Tocci, M., Montesano, L., Gelfi, M., Pola, A. Optimization of heat treatment parameters for additive manufacturing and gravity casting AlSi10Mg alloy. *IOP Conf. Ser. Mater. Sci. Eng.* 2017; **264**; 1-8.

44 Girelli, L., Tocci, M., Gelfi, M., Pola, A. Study of heat treatment parameters for additively manufactured AlSi10Mg in comparison with corresponding cast alloy. *Mater Sci Eng A* 2019: **739**: 317–328.

45 Yang, K.V., Rometsch, P., Davies, C.H.J, Huang, A., Wu, X. Effect of heat treatment on the microstructure and anisotropy in mechanical properties of A357 alloy produced by selective laser melting. *Mater. Des.* 2018; **154**: 275–290.

46 Maskery, I., Aboulkhair, N.T., Corfield, M.R., Tuck, C., Clare, A.T., Leach, R.K., Wildman, R.D., Ashcroft, I.A., Hague, R.J.M Quantification and characterisation of porosity in selectively laser melted Al-Si10-Mg using X-ray computed tomography. *Mater Charact*. 2016; **111**: 193–204.

47 Zhang, B., Li, Y., Bai, Q. Defect Formation Mechanisms in Selective Laser Melting: A Review. *Chinese J. Mech. Eng.* 2017; **30**: 515–527.

48 Romano, S., Brückner-Foit, A., Brandão, A., Gumpinger, J., Ghidini, T., Beretta, S. Fatigue properties of AlSi10Mg obtained by additive manufacturing: Defect-based modelling and prediction of fatigue strength. *Eng Fract Mech* 2018; **187**: 165–189.

49 Paolino, D.S., Tridello, A., Chiandussi, G. and Rossetto, M. S-N curves in the very-high-cycle fatigue regime: statistical modeling based on the hydrogen embrittlement consideration. *Fatigue Fract. Eng. Mater. Struct.* 2016; **39**: 1319-1336.

50 Paolino, D.S., Chiandussi, G., Rossetto, M. A unified statistical model for S-N fatigue curves: probabilistic definition. *Fatigue Fract. Eng. Mater. Struct.* 2013; **36:3**: 187-201.